Hard X-ray Generation from ZnO Nanowire Targets in a Non-Relativistic Regime of Laser-Solid Interactions

Zhanna Samsonova [1,2,3,*], Sebastian Höfer [2], Richard Hollinger [1,2,3], Tino Kämpfer [1], Ingo Uschmann [1,2], Robert Röder [4], Lukas Trefflich [4], Olga Rosmej [5,6], Eckhart Förster [1,2], Carsten Ronning [3,4], Daniil Kartashov [1,3] and Christian Spielmann [1,2,3]

[1] Institute of Optics and Quantum Electronics, Friedrich Schiller University, Jena, Max Wien Platz 1, 07743 Jena, Germany; richard.hollinger@uni-jena.de (R.H.); tinokaempfer@web.de (T.K.); ingo.uschmann@uni-jena.de (I.U.); e.foerster@uni-jena.de (E.F.); daniil.kartashov@uni-jena.de (D.K.); christian.spielmann@uni-jena.de (C.S.)
[2] Helmholtz Institute Jena, Fröbelstieg 3, 07743 Jena, Germany; sebastian@zollsoft.de
[3] Abbe Center of Photonics, Friedrich Schiller University, Jena, Albert Einstein Straße 6, 07745 Jena, Germany; carsten.ronning@uni-jena.de
[4] Institute of Solid State Physics, Friedrich Schiller University, Jena, Helmholtzweg 3, 07743 Jena, Germany; robert.roeder@uni-jena.de (R.R.); lukas.trefflich@uni-leipzig.de (L.T.)
[5] GSI Helmholtz Centre for Heavy Ion Research, Planckstraße 1, 64220 Darmstadt, Germany; o.rosmej@gsi.de
[6] Goethe University, Institute of Applied Physics, Max von Laue Straße 1, 60438 Frankfurt am Main, Germany
[*] Correspondence: zhanna.samsonova@uni-jena.de; Tel.: +49-3641-9-47214

check for updates

Abstract: We present a detailed investigation of X-ray emission from both flat and nanowire zinc oxide targets irradiated by 60 fs 5×10^{16} W/cm^2 intensity laser pulses at a 0.8 μm wavelength. It is shown that the fluence of the emitted hard X-ray radiation in the spectral range 150–800 keV is enhanced by at least one order of magnitude for nanowire targets compared to the emission from a flat surface, whereas the characteristic K_α line emission (8.64 keV) is insensitive to the target morphology. Furthermore, we provide evidence for a dramatic increase of the fast electron flux from the front side of the nanostructured targets. We suggest that targets with nanowire morphology may advance development of compact ultrafast X-ray sources with an enhanced flux of hard X-ray emission that could find wide applications in highenergy density (HED) physics.

Keywords: X-ray generation; laser-matter interaction; ultrashort laser pulses; X-ray spectroscopy; laser plasma emission; nanostructured arrays

1. Introduction

Plasma-based ultrafast X-ray sources are of great importance for many intriguing applications [1]. They provide well-defined line and continuous emission that can be used for time-resolved X-ray spectroscopy of high-density matter. Such ultrashort duration (femtosecond to picosecond time scale) sources of X-ray emission can be designed using an interaction of intense ultrashort laser pulses with solids. At relativistic intensities (>1.3×10^{18} W·μm^2/cm^2), the laser pulse can strongly ionize solid or liquid targets and accelerate electrons beyond 1 MeV [2]. The resulting plasmas act as bright sources of particles (electrons, protons, and neutrons) and X-rays. Corresponding experiments have been carried out at large, joule-energy class, multi-terawatt peak power laser systems with sub-picosecond and, nowadays, femtosecond pulse duration in a single-shot regime [3–7]. However, from a practical point of view of applications in X-ray spectroscopy, high-repetition rate sources of X-rays are of great importance. Therefore, small scale, mJ-level energy, and kHz repetition rate laser systems are

successfully used as drivers for X-ray sources [8–10]. Such portable sources with high brilliance have already been proven to be a powerful tool, e.g., for time-resolved X-ray diffraction [11,12].

Bremsstrahlung emission is often considered as a parasitic background radiation that has to be suppressed. Therefore, insignificant attention has been paid to the investigation into the possibility of effectively generating X-ray photons with energies above 20 keV at a high repetition rate. However, hard X-ray continuous emission has also been used in high-energy density (HED) experiments, such as inertial confinement fusion, in which bremsstrahlung sources are widely used as a "back-lighter" in inverse-bremsstrahlung absorption for time-resolved measurements of electron density [13,14]. Meanwhile, softer bremsstrahlung emission is suitable for X-ray absorption near-edge spectroscopy (XANES) and extended X-ray absorption fine-structure spectroscopy (EXAFS) [15,16].

The bremsstrahlung yield can be enhanced by designing the target's geometry. Nanoparticle coating and specially synthesized nanostructures can greatly increase the X-ray flux [17–19]. It has been shown theoretically that nanoscale structures with optimum parameters, depending on laser pulse duration and intensity, can significantly increase the absorption of laser energy [20,21]. In particular, the nanowire morphology of the target enables deep (much deeper than skin depth) penetration and highly efficient absorption of the laser energy, leading to so-called volumetric heating of the plasma [21]. Consequently, this leads to more efficient generation of hot electrons and, thus, X-ray photons.

In this paper, we report on the experimental investigation of characteristic line and hard X-ray emission generated in ZnO semiconductor nanowire targets of different morphologies, irradiated by ultrashort laser pulses at intensities below 10^{17} W/cm^2. Such intensities at 800 nm wavelength correspond to a non-relativistic interaction, implying that the electron dynamics are not relativistic (the quiver velocity of the electrons in the laser field is smaller than the speed of light). Significant enhancement of the photon flux with energies above several hundred keV (gamma range) and extension of photon energies up to 0.8 MeV is demonstrated. This enhancement is related to the observed dramatic increase in the number and energies of hot electrons generated from nanostructured solid targets.

2. Materials and Methods

The experiments were carried out with a Ti:Sapphire laser system (Quantronix) delivering 60 fs pulses with an energy up to 3.5 mJ (85% of which reaches the target) at the central wavelength of 804 nm and with a 1 kHz repetition rate [22]. The experimental setup is shown schematically in Figure 1a. The laser beam was focused onto the target by a 60° off-axis parabolic mirror (F/1.5) to a 6.8 μm spot (FWHM), providing a peak intensity of 5×10^{16} W/cm^2. The measured nanosecond and picosecond laser pulse contrast was about 10^{-5}–10^{-4}, as determined by the third-order cross-correlation technique. The corresponding fluence of <0.3 J/cm^2 is weak enough to ensure that no pre-plasma can be generated. Therefore, a sharp plasma density gradient was guaranteed. The corresponding Rayleigh length of ≈65 μm is significantly longer than the length of nanowires (NWs). The focal spot was characterized with a standard microscope objective (×20) and a change-coupled device (CCD). The polarization of the laser beam at the target was controlled by a half-wave plate. The incident angle of the laser pulse on the target was fixed at about 40°. The resulting laser pulse intensity on the target surface corresponds to a normalized vector potential $a_0 = eE/m_0\omega c \cong 0.15 \ll 1$, implying non-relativistic interaction. The targets were mounted on an XYZ-translation stage, allowing a new beam position on the target for each laser pulse and change of the target's position along the focus.

The experiment was performed with both nanostructured and bulk zinc oxide (ZnO) targets. This dielectric material is transparent for incident laser radiation at 800 nm, which can promote a volume ionization and extensive exposure to the high-intensity laser field. Wurtzite, single crystalline ZnO nanowire (NW) batches were synthesized using a thermal transport technique within horizontal tube furnaces. We used two different types of nanostructured targets. The first type was an ordered array of NWs consisting of parallel, up-standing NWs perpendicular to the substrate (Figure 1b). The second set of samples contained disordered arrays revealing a batch of NWs chaotically arranged along the

sample surface (Figure 1c). The different morphologies of the structures were achieved by carefully adjusting the growth conditions [23,24]. Briefly, the disordered nanowire samples were synthesized via the vapor-liquid-solid (VLS) mechanism [25] on Si chips covered beforehand with a 10 nm gold layer to act as liquid catalyst droplets during growth. The ordered NW samples were grown self-catalytically using the vapor-solid (VS) approach on a 500 μm thick Si substrate covered with a 500 nm Al-doped ZnO seed layer [26]. The NWs were typically 5 μm and 15 μm long for ordered and disordered NW samples, respectively, and had a diameter of about 100–200 nm.
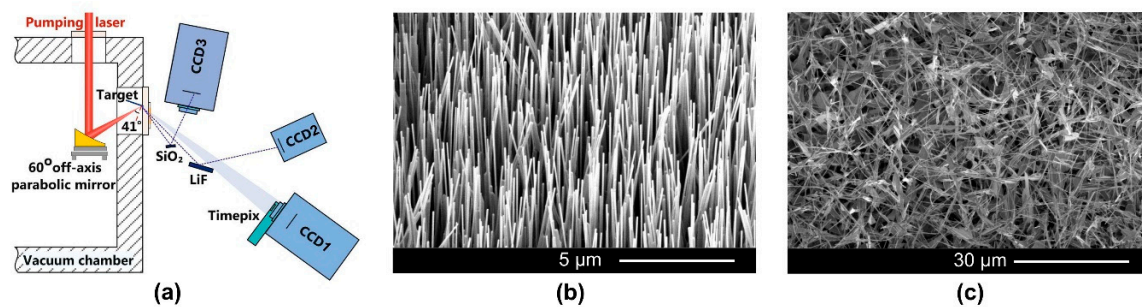
Figure 1. (**a**) the scheme of the experimental setup (not to scale). All the diagnostics (except the focal spot imaging system) are shown. The charge-coupled device (CCD3) recording the X-rays reflected from the quartz (SiO$_2$) crystal also detected signals not reflected from the crystal. Scanning electron microscope (SEM) images of the investigated targets: (**b**) the ordered nanowire (NW) target; (**c**) the disordered NW target.

Since the measurements were done for different polarizations of the laser beam, it is important to explain the direction of polarization with respect to the target morphology (Figure 2). S- and p-polarization are used to refer to the laser pulses with an electric field perpendicular or parallel to the *kn*-plane (the plane of incidence), respectively. Along with their orientation and a finite angle of incidence, p-polarized laser pulses always have a field component $\vec{E_p}\,\vec{n}$ normal to the target surface.
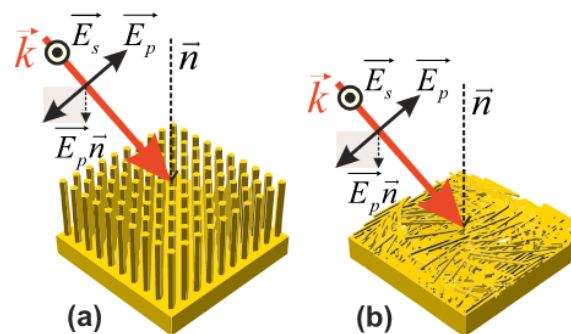

Figure 2. Schematic illustration of the laser field polarization with respect to the target geometry in the case of the ordered NW (**a**) and disordered NW (**b**) samples. $\vec{E_p}$ and $\vec{E_s}$ represent the electric fields of the p- and s- polarized light, respectively. $\vec{n}$ represents the vector normal to the target, and $\vec{k}$ the wave vector of the incident beam.

Reference measurements were carried out with flat, 0.5 μm thick polished ZnO bulk substrates (CrysTec GmbH), which were oriented along the [0001] direction.

The experiments were conducted in a single-shot regime. The area of the target surface was large enough to support over 200 laser pulses for statistical characterization of the results (Figure 3a,b). It can be clearly seen with an optical microscope that the damage spots are nicely separated (Figure 3c). The position of the target with respect to the focus was initially optimized to the highest radiation dose measured with a dosimeter and then tuned to the maximum of the X-ray signal on spectrometers.

The interaction of the laser pulse with the nanostructured and flat targets took place inside a vacuum chamber pumped down to 10^{-4} mbar.
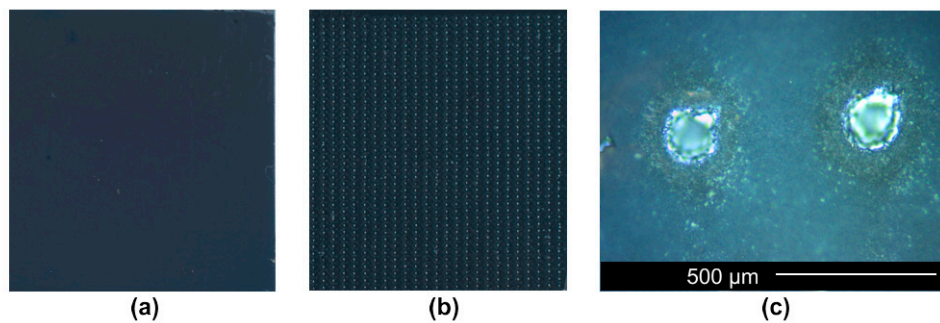
Figure 3. Images of the ordered NW target (**a**) before and (**b**) after interaction with the intense laser pulses. (**c**) optical microscope $50\times$ magnification image of single-shot damage spots on the disordered NW target.

The diagnostic setup was placed outside the chamber in ambient air. The expected line emission and, especially, the hard X-rays were not strongly absorbed on their propagation in air to the detectors at a distance below 1 m. For the line spectrum measurements, two bent crystals were set up. The first one, based on a toroidal quartz (40-4) crystal (2d = 1.672 nm), measured spectra in a narrow spectral window. The spectral resolution was limited by the CCD spatial resolution $\lambda/\delta\lambda < 1500$. This spectrometer enabled a high-resolution investigation of the K_α doublet from zinc.

The second spectrometer, with a cylindrical LiF (220) crystal (2d = 2.848 nm), works in a wide range of energies (from K_α to K_β emission lines of Zn), with a resolution of $\lambda/\delta\lambda < 2000$. The detection of the spectra reflected by the bent crystals was realized by cooled, back-illuminated X-ray CCD cameras (Roper Scientific and Andor, CCD2 and CCD3 in Figure 1a, respectively) with their own vacuum-supporting containers.

For detecting the bremsstrahlung emission, another Andor X-ray CCD camera (CCD1 in Figure 1a), sensitive to photons with energies up to 20 keV, and a Timepix detector were installed. The Timepix detector is based on a 1 mm thick CdTe chip and can register photons with energies from 30 keV to 800 keV [27]. The distance of 45cm from the target was roughly the same for both detectors.

Reliable measurements of bremsstrahlung spectra over a broad range taken with the same CCD camera require correction due to the abruptly decreasing quantum efficiency for higher energies. Additionally, the Compton scattering becomes more important for higher energies, enhancing the count rate. Therefore, for higher energy X-rays, these two counter-acting processes must be carefully considered. The obtained spectra must not only be corrected for absorption in air and the Kapton window but also require additional Monte Carlo simulations considering the two above-mentioned efficiencies scaling with the photon energy (e.g., [28,29]). For our setup, simulations showed that for the given experimental parameters and detected spectra, the introduced correction for the absorption would be sufficient to obtain reliable data. As we used no wavelength dispersive elements for measuring the continuous X-ray spectra, we had to ensure that our detectors operated in the "single-photon counting regime" [30,31], implying, in any case, that the ratio of the number of photons divided by the number of pixels must be ≤ 0.15.

3. Results and Discussion

The X-ray emission spectra in the energy region below 20 keV, detected by the X-ray CCD camera (CCD1), look rather similar for the different target morphologies (Figure 4). The spectra contain the K-shell emission lines of Zn (K_α and K_β) and low-energy bremsstrahlung. The emitted flux from the nanostructured samples, especially from the disordered sample, was barely sensitive to the laser field polarization. In contrast, the signal from the flat sample strongly varied as a function of the polarization

and reached its maximum for p-polarization. The integrated photon flux at Zn K_α was about 1–4×10^6 photons/pulse/sr, which at a 1 kHz repetition rate yielded about 10^{10} photons/s. Comparable X-ray fluxes obtained in similar experimental conditions have been reported [9,22]. Independent of the polarization, the nanostructured targets emitted only slightly more K-shell photons (a factor of 1.3) than the maximum flux value from a polished, flat ZnO target. Following the approach suggested in [32], we applied an exponential fit (Maxwell distribution) to the low-energy bremsstrahlung spectrum in Figure 4 and retrieved an electron temperature of 350–435 eV.
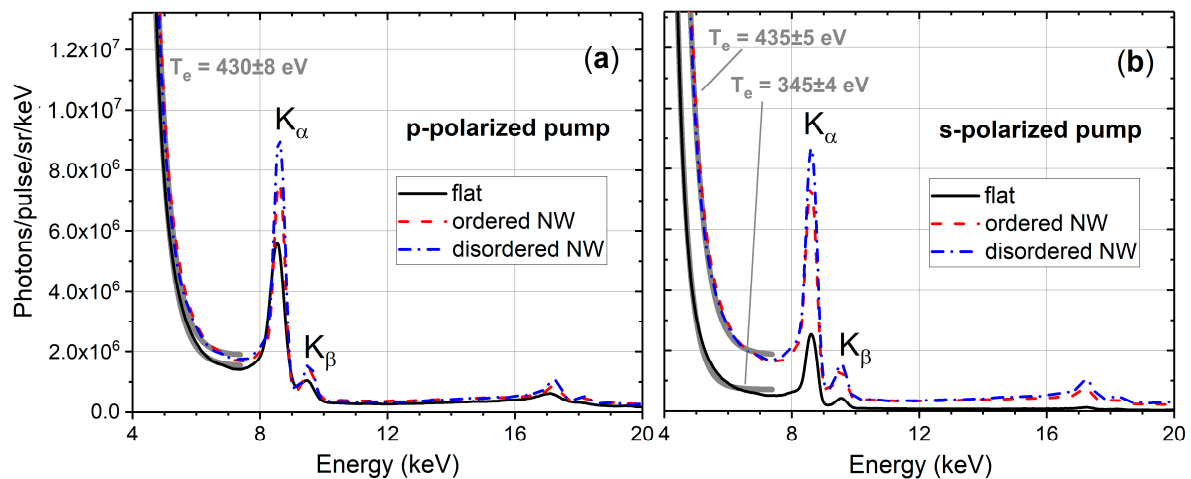
Figure 4. X-ray spectra from the flat (solid black line) and nanostructured (ordered NW (dashed red line) and disordered NW (dash-dotted blue line)) ZnO targets for p-polarization (**a**) and s-polarization (**b**) measured by CCD1 in single photon counting regime. The spectra were fitted with an exponential function (solid grey line), providing an estimation of the electron bulk temperature T_e.

For the high-energy region above 50 keV measured by the Timepix detector, the flux obtained from the ordered and disordered NW samples was significantly stronger than that from the flat sample (see Figure 5). For instance, in the range from 150–350 keV, as marked in Figure 5, we measured a 15 and 22 times higher integrated flux for p-polarized and s-polarized laser pulses, respectively. Also, for these photon energies, the spectra could be fitted using a two-temperature electron energy distribution with corresponding temperatures of 12–15 keV and 40–50 keV (Figure 5). Such several-temperature energy distributions of "hot" electrons in laser generated plasmas have been reported in the past [33–36]. Under conditions of high temporal pulse contrast, as in our experiment, the formation of the pre-plasma is suppressed, which leads to a sharp density profile. In this situation, for oblique incidence of the laser beam, Brunel (or vacuum) heating is the dominant mechanism of laser energy absorption [37–40]. The polarization dependence of the hard X-ray flux in the high-energy region (Figure 5) was similar to the dependence observed for the low-energy region shown in Figure 4. The efficiency of bremsstrahlung X-ray generation in the energy range 50–800 keV is insensitive to the laser polarization in the disordered NW array, weakly sensitive in the ordered NW array, and strongly sensitive in the flat target. This difference can be understood by considering the geometry of interaction schematically shown in Figure 2. When the electric field of the pump laser has only a tangential component (s-polarization), the vacuum heating is suppressed, which explains the experimental results for the flat surface. Meanwhile, for NW morphologies, for any laser beam polarization there is always a component of the field perpendicular to the surface of a NW. Thus, it is obvious that for s-polarized light, the vertically standing and ordered NWs were more efficient emitters of hard X-ray photons than the flat bulk sample (6-fold enhancement for 150–350 keV). Despite the observed electron heating with s-polarized light, for the ordered morphology the p-polarized light could still transfer energy to the electrons more efficiently, resulting in a higher flux. In contrast, for disordered targets it seems that the polarization played no role, while at any orientation of polarization

there was always a component of the field normal to the local plasma gradient and responsible for the efficient generation of electrons causing bremsstrahlung. A rough estimation of the hard X-ray flux in the range 150–350 keV gave up to 10^6 photons/pulse in 4π. Our observations are in agreement with recent studies using copper nanorods with similar length to our NWs (10 μm). Despite the higher average density of the Cu target material [41], the reported X-ray flux was similar to that in our experiments.
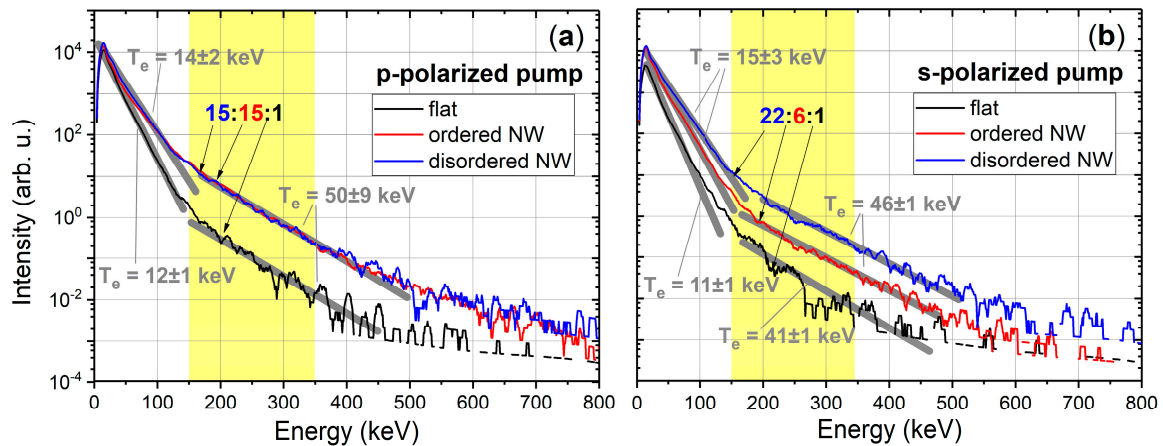

Figure 5. Hard X-ray spectra from the flat (black line), ordered (red line), and disordered (blue line) nanostructured ZnO targets for p-polarization (**a**) and s-polarization (**b**) measured by the Timepix detector. Relation of the hard X-ray flux is given for the marked (yellow) energy range. The spectra were fitted with an exponential function (solid grey line) providing an estimation of the electron "hot" temperatures T_e.

The K-shell emission spectra, measured with two crystal spectrometers for all investigated samples, are shown in Figure 6. The observed lines correspond to the K-L (K_α) and K-M (K_β) transitions in cold material. Note that K_α and K_β emission from ion states up to Zn^{20+} (Ne-like Zn) strongly overlap and cannot be resolved with our spectrometers. Therefore, line spectra in Figure 6 could be a superposition of line emissions from transient charge states up to 20+ and suggest that no Zn ions with a charge state higher than 20+ were generated under the conditions of our experiments. The polarization dependence of the line spectra is similar to the dependence observed for the bremsstrahlung radiation: The disordered NW target showed the same efficiency for all polarization directions, the ordered NW target demonstrated a weak polarization dependence, and the flat target was strongly sensitive to the laser polarization. Comparing the dependence of the line emission and high-energy bremsstrahlung radiation on the target morphology (Figures 5 and 6), we conclude that, in contrast to high-energy photons, no significant enhancement in the characteristic emission (also known as "cold" emission) for NW arrays was observed. This result can be explained as follows. The yield of the continuum of bremsstrahlung emission in the range of quanta energy below 100 keV is essentially the same, or very similar, for polished and nanostructured targets (see Figures 4 and 5). Therefore, the density of electrons with similar kinetic energies should be comparable for all types of targets. However, these are the electrons contributing the most in the generation of the K_α emission in Zn [42].

Therefore, despite the assumed deeper penetration of the laser pulse into the NW targets and volumetric heating, the yield of the K_α emission was not enhanced because of reabsorption. Additionally, the hot electrons could go far into the target volume (12 μm for 50 keV electrons) creating the K-shell holes. However, in the case of the NW targets, the substrate was made of Si,, and thus this volume did not make any contribution to the Zn K_α. Concluding the results on K_α emission, it is noteworthy that the ratios of the integrated K_α fluxes from the investigated ZnO targets, calculated from the data measured with two crystal spectrometers and directly with the CCD camera (CCD1),

were in close agreement with each other. The mean values for the relative K yield are given in Table 1. It is worth mentioning that the observed polarization dependence for the K_α emission had the same origin as the bremsstrahlung emission discussed above, since both types of radiation are related to the generation of hot electrons.
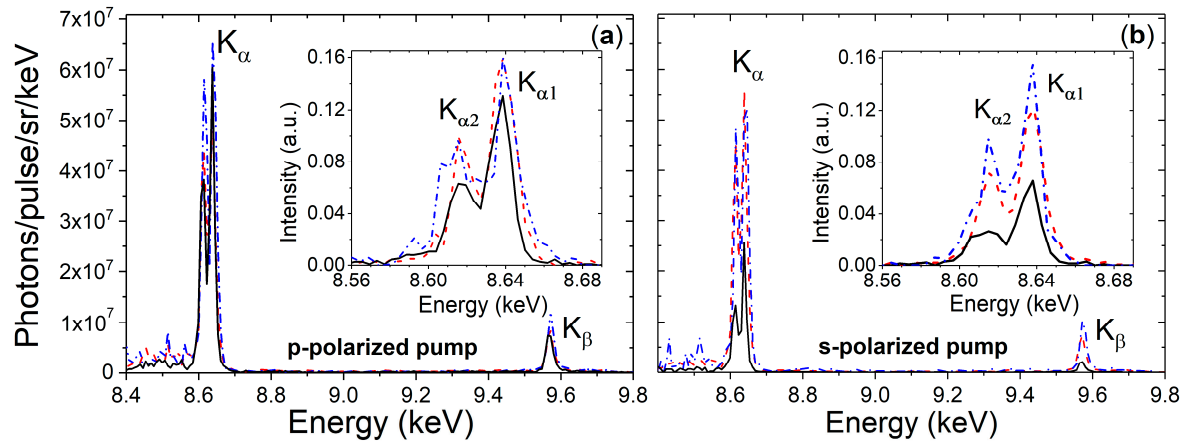

Figure 6. The K-shell emission and K_α doublet (insets) from ZnO targets (flat (black line), ordered NW (red line), and disordered NW (blue line)) detected with LiF (220) and quartz (40-4) bent crystal spectrometer, respectively. The spectra were obtained from interaction with a p-polarized (**a**) and s-polarized (**b**) laser beam.

Table 1. The mean values of the integrated Zn K_α emission for the investigated targets obtained with p- and s-polarized laser pulse. The values are normalized on the integrated Zn K_α flux from the flat sample.

	Flat	Ordered NW	Disordered NW
p-polarization	1	1.19 ± 0.04	1.31 ± 0.05
s-polarization	1	2.79 ± 0.11	3.18 ± 0.08

Finally, the X-ray CCD camera used for the line emission detection in the quartz crystal spectrometer (CCD1 in Figure 1a) also detected quite intense background bremsstrahlung radiation homogeneously covering the chip. To investigate the origin of this strong background radiation, we performed several tests. (1) We blocked the quartz crystal, so that no emission could be generated or reflected from it. No change in the measured signal was observed in this case. (2) We placed a 2 mm Al foil at the output Kapton window of the experimental vacuum chamber. The background radiation disappeared completely. Since the foil is highly transparent (the transmission efficiency is >70%) for X-ray quanta with energies above 30 keV, we concluded that the observed emission was generated by fast electrons emitted through the Kapton window. The possibility for direct hits on the CCD chip by electrons was excluded, because forward accelerated electrons were shielded by the 2.5 cm thick Al wall of the vacuum chamber (see Figure 1a). Thus, we suggest that the background emission with the spectrum shown in Figure 7 was a bremsstrahlung emission generated by energetic electrons that radiatively lost their energy when interacting with air. Using data for the radiative stopping power of electrons in air [43], we estimated that the spectra in Figure 7 could be emitted by electrons with kinetic energies above 100 keV. Therefore, Figure 7a suggests that, in the case of p-polarization, which was the most favorable for the flat target, ordered nanowire arrays enable nearly two orders of magnitude and disordered arrays nearly one order of magnitude enhancement in the amount of high-energy electrons. This enhancement can be explained by the much higher efficiency of the laser energy absorption and much larger volume of the plasma (volumetric heating effect) for nanowire morphology in comparison to a flat surface. Again, the polarization dependence of the spectra in Figure 7 shows that the efficiency of fast electron generation was essentially insensitive in

the disordered NW arrays, was weakly sensitive in ordered arrays, and was strongly sensitive to the laser polarization for the flat surface.
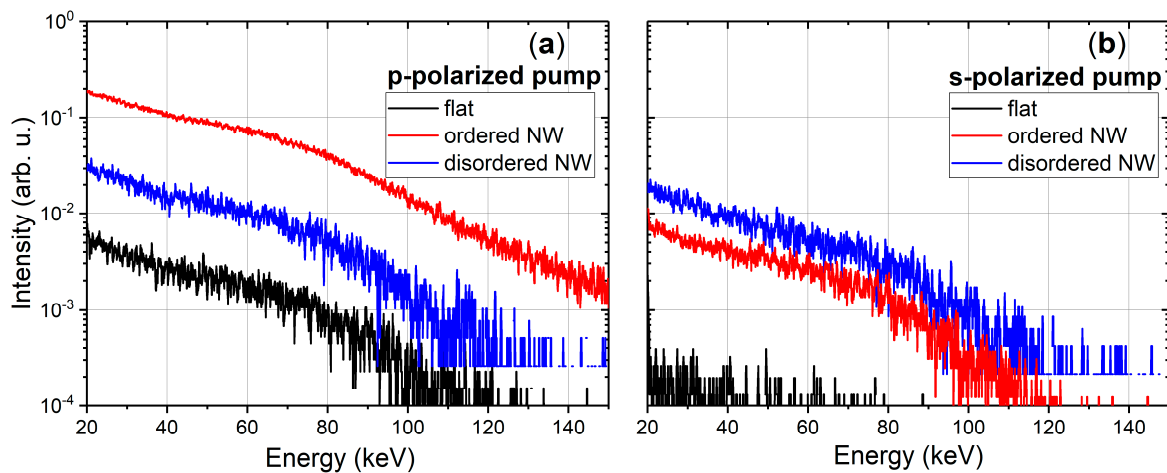
Figure 7. The background signal from the flat (black line) and nanostructured (ordered NW (red line), disordered NW (blue line)) ZnO targets for p-polarization (**a**) and s-polarization (**b**) detected by the CCD camera (CCD1).

4. Conclusions

We have experimentally investigated the influence of ZnO target morphology on X-ray emission under illumination with several-mJ femtosecond laser pulses focused to intensities $< 10^{17}$ W/cm^2. Replacing flatsurface targets with NW arrays enables enhancement of the hard X-ray flux by 15–22 times in the energy range of 150–300 keV. This enhancement can be explained by a much higher efficiency of laser energy absorption in NW arrays, resulting in a significant increase of the number and energies of hot electrons. In contrast, no significant increase was detected in the "cold" Zn K-shell emission, which can be attributed to the lower material density, the different material of the substrate, and reabsorption effects in a larger volume of generation. The polarization dependence of the photon flux supports the assumption that vacuum heating is the main mechanism responsible for X-ray generation. It was shown that the efficiency of X-ray generation in NW arrays is weakly sensitive to laser polarization, in contrast to the flat surface. These experimental results allow the conclusion that there are no strict requirements for incidence geometry, nor for laser beam polarization when disordered NW targets are utilized. Examination of these targets in interactions with non-relativistic laser pulses was an essential step towards gaining a better understanding of the phenomena to be expected at higher intensities. We believe that our results may contribute to the development of efficient hard X-ray sources at kHz repetition rate driven by moderate-intensity lasers and are of great importance for many applications in X-ray spectroscopy.

Author Contributions: Z.S. and S.H. carried out experiments, data processing, and numerical simulations; T.K., I.U., and E.F. contributed to experimental measurements and X-ray spectroscopy; R.R., L.T., and C.R. provided the nanowires and contributed to the discussion of the results; I.U., O.R., E.K., C.R., D.K., and C.S. contributed to the discussion and interpretation of the results; Z.S., D.K., and C.S. wrote the paper with contributions from other authors. R.H. contributed to experimental measurements and X-ray spectroscopy

References

1. Rousse, A.; Rischel, C.; Gauthier, J.-C. Ultrafast X-ray sources and applications. *Comptes Rendus de l'Académie des Sciences-Series IV-Physics* **2000**, *1*, 305–315. [CrossRef]
2. Umstadter, D. Relativistic laser–Plasma interactions. *J. Phys. D Appl. Phys.* **2003**, *36*, R151. [CrossRef]
3. Beg, F.N.; Bell, A.R.; Dangor, A.E.; Danson, C.N.; Fews, A.P.; Glinsky, M.E.; Hammel, B.A.; Lee, P.; Norreys, P.A.; Tatarakis, M. A study of picosecond laser–Solid interactions up to 10^{19} W cm^{-2}. *Phys. Plasmas* **1997**, *4*, 447–457. [CrossRef]
4. Cowan, T.E.; Hunt, A.W.; Phillips, T.W.; Wilks, S.C.; Perry, M.D.; Brown, C.; Fountain, W.; Hatchett, S.; Johnson, J.; Key, M.H.; et al. Photonuclear fission from high energy electrons from ultraintense laser-solid interactions. *Phys. Rev. Lett.* **2000**, *84*, 903–906. [CrossRef] [PubMed]
5. Schwoerer, H.; Gibbon, P.; Düsterer, S.; Behrens, R.; Ziener, C.; Reich, C.; Sauerbrey, R. MeV X rays and photoneutrons from femtosecond laser-produced plasmas. *Phys. Rev. Lett.* **2001**, *86*, 2317–2320. [CrossRef] [PubMed]
6. Park, H.-S.; Chambers, D.M.; Chung, H.-K.; Clarke, R.J.; Eagleton, R.; Giraldez, E.; Goldsack, T.; Heathcote, R.; Izumi, N.; Key, M.H.; et al. High-energy Kα radiography using high-intensity, short-pulse lasers. *Phys. Plasmas* **2006**, *13*, 056309. [CrossRef]
7. Fourmaux, S.; Kieffer, J.C. Laser-based K_α X-ray emission characterization using a high contrast ratio and high-power laser system. *Appl. Phys. B* **2016**, *122*, 162. [CrossRef]
8. Hagedorn, M.; Kutzner, J.; Tsilimis, G.; Zacharias, H. High-repetition-rate hard X-ray generation with sub-millijoule femtosecond laser pulses. *Appl. Phys. B* **2003**, *77*, 49–57. [CrossRef]
9. Zamponi, F.; Ansari, Z.; Korff Schmising, C.V.; Rothhardt, P.; Zhavoronkov, N.; Woerner, M.; Elsaesser, T.; Bargheer, M.; Trobitzsch-Ryll, T.; Haschke, M. Femtosecond hard X-ray plasma sources with a kilohertz repetition rate. *Appl. Phys. A* **2009**, *96*, 51–58. [CrossRef]
10. Holtz, M.; Hauf, C.; Weisshaupt, J.; Salvador, A.-A.H.; Woerner, M.; Elsaesser, T. Towards shot-noise limited diffraction experiments with table-top femtosecond hard x-ray sources. *Struct. Dyn.* **2017**, *4*, 054304. [CrossRef]
11. Silies, M.; Witte, H.; Linden, S.; Kutzner, J.; Uschmann, I.; Förster, E.; Zacharias, H. Table-top kHz hard X-ray source with ultrashort pulse duration for time-resolved X-ray diffraction. *Appl. Phys. A* **2009**, *96*, 59–67. [CrossRef]
12. Höfer, S.; Kämpfer, T.; Förster, E.; Stöhlker, T.; Uschmann, I. The formation of rarefaction waves in semiconductors after ultrashort excitation probed by grazing incidence ultrafast time-resolved x-ray diffraction. *Struc. Dyn.* **2016**, *3*, 051101. [CrossRef] [PubMed]
13. Park, H.-S.; Maddox, B.R.; Giraldez, E.; Hatchett, S.P.; Hudson, L.T.; Izumi, N.; Key, M.H.; Le Pape, S.; MacKinnon, A.J.; MacPhee, A.G.; et al. High-resolution 17–75 keV backlighters for high energy density experiments. *Phys. Plasmas* **2008**, *15*, 072705. [CrossRef]
14. Remington, B.A.; Rudd, R.E.; Wark, J.S. From microjoules to megajoules and kilobars to gigabars: Probing matter at extreme states of deformation. *Phys. Plasmas* **2015**, *22*, 090501. [CrossRef]
15. Benesch, F.; Lee, T.W.; Jiang, Y.; Rose-Petruck, C.G. Ultrafast laser-driven x-ray spectrometer for x-ray absorption spectroscopy of transition metal complexes. *Opt. Lett.* **2004**, *29*, 1028–1030. [CrossRef] [PubMed]
16. Fullagar, W.; Harbst, M.; Canton, S.; Uhlig, J.; Walczak, M.; Wahlström, C.-G.; Sundström, V. A broadband laser plasma x-ray source for application in ultrafast chemical structure dynamics. *Rev. Sci. Instrum.* **2007**, *78*, 115105. [CrossRef] [PubMed]
17. Kulcsár, G.; AlMawlawi, D.; Budnik, F.W.; Herman, P.R.; Moskovits, M.; Zhao, L.; Marjoribanks, R.S. Intense picosecond X-Ray pulses from laser plasmas by use of nanostructured "Velvet" targets. *Phys. Rev. Lett.* **2000**, *84*, 5149–5152. [CrossRef]
18. Rajeev, P.P.; Banerjee, S.; Sandhu, A.S.; Issac, R.C.; Tribedi, L.C.; Kumar, G.R. Role of surface roughness in hard-X-ray emission from femtosecond-laser-produced copper plasmas. *Phys. Rev. A* **2002**, *65*, 052903. [CrossRef]
19. Rajeev, P.P.; Taneja, P.; Ayyub, P.; Sandhu, A.S.; Ravindra Kumar, G. Metal nanoplasmas as bright sources of hard X-Ray pulses. *Phys. Rev. Lett.* **2003**, *90*, 115002. [CrossRef] [PubMed]
20. Andreev, A.A.; Platonov, K.Y. Interaction of ultra high intensity laser pulse with structured target and fast particle generation in a stable mode. *Contrib. Plasma Phys.* **2013**, *53*, 173–178. [CrossRef]

21. Purvis, M.A.; Shlyaptsev, V.N.; Hollinger, R.; Bargsten, C.; Pukhov, A.; Prieto, A.; Wang, Y.; Luther, B.M.; Yin, L.; Wang, S.; et al. Relativistic plasma nanophotonics for ultrahigh energy density physics. *Nat. Photonics* **2013**, *7*, 796–800. [CrossRef]

22. Uschmann, I.; Kämpfer, T.; Zamponi, F.; Lübcke, A.; Zastrau, U.; Loetzsch, R.; Höfer, S.; Morak, A.; Förster, E. Investigation of fast processes in condensed matter by time-resolved x-ray diffraction. *Appl. Phys. A* **2009**, *96*, 91–98. [CrossRef]

23. Borchers, C.; Stichtenoth, D.; Müller, S.; Schwen, D.; Ronning, C. Catalyst−Nanostructure interaction in the growth of 1-D ZnO nanostructures. *J. Phys. Chem. B* **2016**, *110*, 1656–1660. [CrossRef] [PubMed]

24. Johannes, A.; Noack, S.; Paschoal, W., Jr.; Kumar, S.; Jacobsson, D.; Pettersson, H.; Samuelson, L.; Dick, K.A.; Martinez-Criado, G.; Burghammer, M.; et al. Enhanced sputtering and incorporation of Mn in implanted GaAs and ZnO nanowires. *J. Phys. D* **2014**, *47*, 394003. [CrossRef]

25. Wagner, R.S.; Ellis, W.C. Vapor-liquid-solid mechanism of single crystal growth. *Appl. Phys. Lett.* **1964**, *4*, 89–90. [CrossRef]

26. Yang, P.; Yan, H.; Mao, S.; Russo, R.; Johnson, J.; Saykally, R.; Morris, N.; Pham, J.; He, R.; Choi, H.-J. Controlled Growth of ZnO Nanowires and Their Optical Properties. *Adv. Funct. Mater.* **2002**, *12*, 323–331. [CrossRef]

27. Hahn, C.; Weber, G.; Märtin, R.; Höfer, S.; Kämpfer, T.; Stöhlker, T. CdTe Timepix detectors for single-photon spectroscopy and linear polarimetry of high-flux hard x-ray radiation. *Rev. Sci. Instrum.* **2016**, *87*, 043106. [CrossRef]

28. Sjögren, A.; Harbst, M.; Wahlström, C.-G.; Svanberg, S.; Olsson, C. High-repetition-rate, hard x-ray radiation from a laser-produced plasma: Photon yield and application considerations. *Rev. Sci. Instrum.* **2003**, *74*, 2300–2311. [CrossRef]

29. Chen, C.D.; Patel, P.K.; Hey, D.S.; Mackinnon, A.J.; Key, M.H.; Akli, K.U.; Bartal, T.; Beg, F.N.; Chawla, S.; Chen, H.; et al. Bremsstrahlung and Kα fluorescence measurements for inferring conversion efficiencies into fast ignition relevant hot electrons. *Phys. Plasmas* **2009**, *16*, 082705. [CrossRef]

30. Lötzsch, R.; Jäckel, O.; Höfer, S.; Kämpfer, T.; Polz, J.; Uschmann, I.; Kaluza, M.C.; Förster, E.; Stambulchik, E.; Kroupp, E.; et al. K-shell spectroscopy of silicon ions as diagnostic for high electric fields. *Rev. Sci. Instrum.* **2012**, *83*, 113507. [CrossRef]

31. Livet, F.; Bley, F.; Mainville, J.; Caudron, R.; Mochrie, S.G.J.; Geissler, E.; Dolino, G.; Abernathy, D.; Grübel, G.; Sutton, M. Using direct illumination CCDs as high-resolution area detectors for X-ray scattering. *Nucl. Instrum. Methods Phys. Res. A* **2000**, *451*, 596–609. [CrossRef]

32. McCall, G.H. Calculation of X-ray bremsstrahlung and characteristic line emission produced by a Maxwellian electron distribution. *J. Phys. D* **1982**, *15*, 823. [CrossRef]

33. Rosmej, O.N.; Samsonova, Z.; Höfer, S.; Kartashov, D.; Arda, C.; Khaghani, D.; Schoenlein, A.; Zähter, S.; Hoffmann, A.; Loetzsch, R.; et al. Generation of keV hot near-solid density plasma states at high contrast laser-matter interaction. *Phys. Plasmas* **2018**, *25*, 083103. [CrossRef]

34. Ivanov, K.; Shulyapov, S.; Turinge, A.; Brantov, A.; Uryupina, D.; Volkov, R.; Rusakov, A.; Djilkibaev, R.; Nedorezov, V.; Bychenkov, V.; et al. X-Ray Diagnostics of Ultrashort Laser-Driven Plasma: Experiment and Simulations. *Contrib. Plasma Phys.* **2013**, *53*, 116–121. [CrossRef]

35. Sherlock, M. Universal scaling of the electron distribution function in one-dimensional simulations of relativistic laser-plasma interactions. *Phys. Plasmas* **2009**, *16*, 103101. [CrossRef]

36. Burnett, N.H.; Enright, G.D. Hot-electron generation and transport in high-intensity laser interaction. *Can. J. Phys.* **1986**, *64*, 920–931. [CrossRef]

37. Brunel, F. Not-so-resonant, resonant absorption. *Phys. Rev. Lett.* **1987**, *59*, 52–55. [CrossRef] [PubMed]

38. Gibbon, P.; Bell, A.R. Collisionless absorption in sharp-edged plasmas. *Phys. Rev. Lett.* **1992**, *68*, 1535–1538. [CrossRef] [PubMed]

39. Mulser, P.; Weng, S.M.; Liseykina, T. Analysis of the Brunel model and resulting hot electron spectra. *Phys. Plasmas* **2012**, *19*, 043301. [CrossRef]

40. Liseykina, T.; Mulser, P.; Murakami, M. Collisionless absorption, hot electron generation and energy scaling in intense laser-target interaction. *Phys. Plasmas* **2015**, *22*, 033302. [CrossRef]

41. Mondal, S.; Chakraborty, I.; Ahmad, S.; Carvalho, D.; Singh, P.; Lad, A.D.; Narayanan, V.; Ayyub, P.; Ravindra Kumar, G.; Zheng, J.; et al. Highly enhanced hard x-ray emission from oriented metal nanorod arrays excited by intense femtosecond laser pulses. *Phys. Rev. B* **2011**, *83*, 035408. [CrossRef]

42. Salzmann, D.; Reich, C.; Uschmann, I.; Förster, E.; Gibbon, P. Theory of K$_\alpha$ generation by femtosecond laser-produced hot electrons in thin foils. *Phys. Rev. E* **2002**, *65*, 036402. [CrossRef] [PubMed]

43. Berger, M.J.; Coursey, J.S.; Zucker, M.A.; Chang, J. *PSTAR, and ASTAR: Computer Programs for Calculating Stopping-Power and Range Tables for Electrons, Protons, and Helium Ions (Version 1.2.3)*; National Institute of Standards and Technology: Gaithersburg, MD, USA, 2005; Volume 39. Available online: http://physics.nist.gov/Star (accessed on 10 July 2018).